FINAL REPORT

Project Title:	A Combined Experimental and Computational Approach for the Design of Mold Surface Topography that Leads to Desired Ingot Surface and Microstructure in Aluminum Casting.
Covering period:	8/31/02 - 8/31/05
Date of Report:	30 September 2005
Recipient:	Cornell University
Award Number:	DE-FC07-02ID14396
SubContractors:	None
Other Partners:	Alcoa
Contact(s) :	Prof. Nicholas Zabaras Phone: (607)-255-9104 Email: zabaras@cornell.edu
Project Team:	**Cornell University**: Prof. N. Zabaras (PI), Deep Samanta (Graduate Student) and Lijian Tan (Graduate Student) **Alcoa**: Dr. Alvaro Giron (Research Engineer)
Project Objective:	A design methodology will be developed with which casting mold surface topographies can be tuned to produce required surface features and micro-structural properties of Aluminum ingots. Both static and continuous casting processes will be examined with instrumented molds. Mold surface topographies, which consist of unidirectional and bi-directional groove textures, will be generated using contact and non-contact techniques to elicit a radiator-like effect at the mold-casting interface.

Background: The rate of heat extraction, the evolution of near-surface cast microstructure, and shell macro-morphology can be controlled once the proper balance between mold surface area extension and the degree of imperfect wetting at the instant solidification starts is determined. Once this control is achieved, it will be possible to minimize or even eliminate costly post-casting surface milling or scalping which is currently a major barrier to the development of new Aluminum casting processes.

1 Executive summary

The current project has investigated the process of surface defect formation in cast aluminum alloys through extensive numerical studies with the main aim of developing methodologies to reduce surface defects in castings by designing appropriate mold surface topologies. These techniques can help reduce material, energy and monetary losses during post-scalping operations. A robust stabilized finite element based alloy solidification simulator was first built and was extended to model the deformation of solidifying alloys in the presence of non-uniform contact and non-uniform heat transfer at the metal mold interface. The mold surface topography was modeled in the form of sinusoidal surfaces and the effect of uneven surface topography on the solidification process was examined first. After initial verification and validation of the numerical model, full scale parametric analysis was performed to study the effect of various process parameters on the deformation of an aluminum alloy solidifying on uneven surfaces. Optimal surface features were identified that helped in reducing some surface defects like growth front unevenness in cast aluminum alloys. Our analysis, first done on the macro-scale, was then extended to the micro-scale where effects of surface tension on air-gap formation and solidification were examined. Level set methods, previously used for modeling dendritic solidification of metals and alloys, were used for this purpose.

The current approach has led to a better understanding of the phenomena occurring during the early stages of aluminum alloy solidification. Numerical studies done in this project form the basis for any surface modification techniques used in molds to reduce or eliminate surface defects in cast aluminum alloys. These techniques when implemented in the industry will lead to material, monetary and energy savings.

2 Project Accomplishments

- Development of a robust alloy solidification simulator for modeling complex alloy solidification processes.
- Numerical study of aluminum alloy solidification on sinusoidal surfaces.
- Development of a coupled simulator to model the deformation of solidifying aluminum and aluminum alloys in the presence of air-gap formation and non-uniform heat transfer.
- Full scale parametric analysis to study the effect of uneven surface topography and various process parameters on early stage solidification of pure aluminum and aluminum-copper (Al-Cu) alloys.

- Determination of optimal surface features that help in minimizing some surface defects in solidifying Al-Cu alloys.
- Numerical study of the effect of surface tension on early stage solidification using *Surface Evolver*.
- Development of highly robust level-set methods to model dendritic alloy solidification and evolution of surfaces in contact.
- Study of surface tension and gas pressure on early stage solidification using level set methods.
- Development of PETSc based parallel solution techniques.

3 Project Activities

3.1 Introduction

During the early stages of solidification of aluminum alloys, phenomena occurring at the solid-shell/mold interface have a direct influence on the formation of surface defects such as cracks, liquation and inverse segregates. This in turn has profound influence on the final macro-morphology and microstructure of the cast alloy. Removal of surface defects from castings leads to large material, monetary and energy losses. One of the main motivations of the current study was to obtain a detailed understanding of the surface-defect formation process in cast Aluminum alloys and explore the role of tuned mold surface topographies to minimize or eliminate these defects.

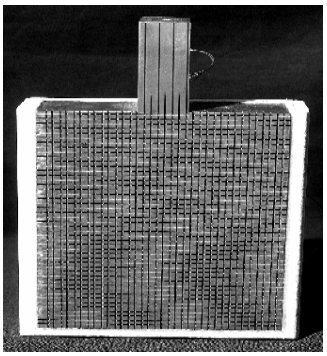

Figure 1: A mold surface with periodic 'groove' topography to control heat extraction during directional solidification (courtesy ALCOA Corp.)

Heat transfer at the metal-mold interface, thermal stress development, imperfect contact, air-gap nucleation, fluid flow and segregation are typical phenomena that occur at the early stages of solidification. Mold surface unevenness plays an important role during early stages of solidification and can influence the growth morphology and microstructure of the solid-shell. Very often in the casting industry, mold surfaces are given an artificial topography to enhance heat transfer and wettability characteristics. These topographies generally range from unidirectional grooves to discrete recessions or cavities. A periodic mold surface topography on the surface of a copper mold block used for immersion studies is shown in Fig. 1 with the experimental details given in [1]. The surface topography depicted in Fig. 1 is a bi-directional counterpart of the unidirectional topography modeled in the present work for stationary molds.

Box I : Governing transport equations for solidification of alloys

$$\frac{\partial \rho}{\partial t} + \nabla \cdot (\rho \boldsymbol{v}) = 0, \qquad (\boldsymbol{x}, t) \in \Omega \times [0, t_{max}], \tag{1}$$

$$\frac{\partial (\rho \boldsymbol{v})}{\partial t} + \nabla \cdot \left(\frac{\rho \boldsymbol{v} \boldsymbol{v}}{f_l} \right) = -\nabla p + \frac{p}{\epsilon_l} \nabla \epsilon_l - \frac{\epsilon_l \rho \mu_l}{\rho_l K(\epsilon_l)} \boldsymbol{v} + \frac{\mu_l}{\rho_l} \nabla \cdot \left[\nabla (\rho \boldsymbol{v}) + (\nabla (\rho \boldsymbol{v}))^t \right],$$

$$\epsilon \rho_0 g [\beta_{l,T} (T - T_0) + \beta_{l,C} (C_l - C_{l_0})] \ \boldsymbol{e_g}, \quad (\boldsymbol{x}, t) \in \Omega \times [0, t_{max}], \tag{2}$$

$$\rho c^* \frac{\partial T}{\partial t} + \rho c_l \boldsymbol{v} \cdot \nabla T = \nabla \cdot [(\epsilon_l k_l + \epsilon_s k_s) \nabla T]$$

$$-\rho_s \left((c_l - c_s)(T - T_e) + h_f \right) \frac{\partial \epsilon_l}{\partial t}, \ (\boldsymbol{x}, t) \in \Omega \times [0, t_{max}], \tag{3}$$

$$\frac{\partial (\rho C)}{\partial t} + \nabla \cdot (\rho \boldsymbol{v} C_l) = \nabla \cdot (\rho f_l D_l \nabla C_l), \qquad (\boldsymbol{x}, t) \in \Omega \times [0, t_{max}], \tag{4}$$

Initial conditions:

$$\boldsymbol{v}(\boldsymbol{x}, 0) = \boldsymbol{0}, \quad T(\boldsymbol{x}, 0) = T_i, \quad C(\boldsymbol{x}, 0) = C_i, \quad \rho(\boldsymbol{x}, 0) = \rho_{l_0}, \quad \frac{\rho(\boldsymbol{x}, 0)}{\rho_l} = 1.0 \ \ \boldsymbol{x} \in \Omega, \tag{5}$$

The periodic groove topography allows multi-directional heat flow at the mold/shell interface. The pitch or wavelength must be on the millimeter scale to obtain anticipated benefits. The main focus of the current work was to explore the role of uneven mold surface topographies during the solidification of aluminum alloys.

3.2 Mathematical Model for Alloy Solidification Problem

Directional solidification of an Al-Cu alloy on sinusoidal molds of wavelength, λ, and amplitude, A, as shown in Fig. 2, was first considered. A single domain model based on volume-averaged governing transport equations is used for modeling solidification of the alloy. The single set of governing transport equations, valid throughout the domain, are listed in Box I. The mushy-zone permeability, K, is assumed to be isotropic and is given by the Kozeny-Carman relation as:

$$K(\epsilon_l) = \frac{K_0 \epsilon_l^3}{(1 - \epsilon_l)^2}, \tag{6}$$

where ϵ_l denotes the volume fraction of liquid. The parameter K_0 is related to the secondary dendrite arm spacing, d, as $K_0 = d^2/180$. In the two-phase mushy-zone, the total solute concentration, C, is expressed in terms of the individual phase concentrations as

$$C = f_l C_l + f_s C_s, \tag{7}$$

where C_l is the solute concentration in the liquid phase, while C_s is the solute concentration in the solid phase. f_l and f_s denote the corresponding mass fractions. The density in the mushy-zone is given by

$$\rho = \rho_l \epsilon_l + \rho_s \epsilon_s, \tag{8}$$

where ρ_s and ρ_l denote the densities of the solid and liquid phases, respectively, while ϵ_s denotes the solid volume fraction. We assume the conservation of both mass and volume in our domain. Volume fractions are related to the respective mass fractions as $\epsilon_l = \rho f_l / \rho_l$ and

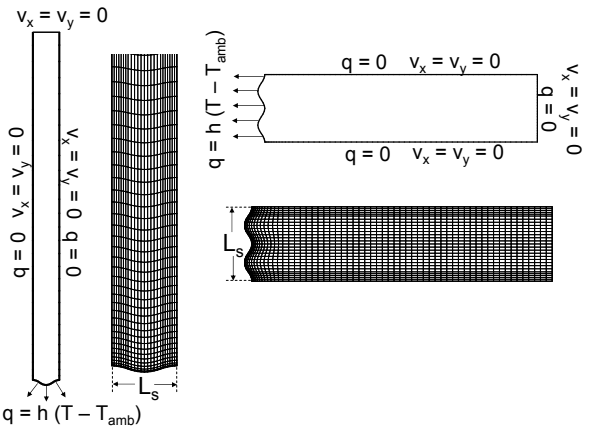

Figure 2: Domain and the mesh for the solidification of aluminum alloy.

$\epsilon_s = \rho f_s/\rho_s$. Closure of the numerical model is achieved through separate thermodynamic relationships describing the evolution of the liquid mass fraction. These are listed below:

$$\text{Lever rule} : f_l = 1 - \frac{1}{1-\kappa_p}\left(\frac{T - T_{liq}}{T - T_m}\right), \tag{9}$$

$$\text{Scheil rule} : f_l = \left(\frac{T - T_m}{T_{liq} - T_m}\right)^{\frac{1}{k_p - 1}}, \tag{10}$$

The Lever rule was used for examples considered in this section. Air-gap formation and stress development in the solid and mushy zones were initially not modeled. The heat transfer at the metal-mold interface was assumed to be uniform here.

3.3 Solution Techniques and Numerical Examples

Stabilized finite element techniques are used in discretizing governing transport equations for alloy solidification. The stabilized solution method for fluid flow incorporates the effect of advection, viscous, pressure and Darcy terms, while those for heat and solute transport are based on the SUPG solution method. Details of these techniques and stabilizing terms involved are given in [2] and [3]. Solidification of an Al-Cu alloy was simulated on uneven surfaces characterized by sinusoidal curves of different wavelengths and amplitudes. The main aim here was to study the effect of uneven surface topography on heat transfer, phase change, fluid flow and macrosegregation in the solidifying alloy. Examples were carried out in both the horizontal and vertical configurations. Figure 2 shows the problem domain and the boundary conditions. Further details are given in [4] and are not repeated here. The surfaces from where heat is removed by convective cooling were modeled as sinusoids and the reference example for both configurations was solidification in a perfectly rectangular cavity of same dimensions. Variation of inverse segregation, macrosegregation and fluid flow with surface topography was studied in all these examples and some important observations were drawn. Figs. 3-4 show the temperature, liquid volume fraction and liquid solute concentration contours for few amplitude-wavelength (A-λ) combinations. Figs. 5-6 show the variation of solute (Cu) concentration for different A-λ combinations. Figs. 7-8 show the temperature, Cu concentration, liquid solute concentration and liquid volume fraction contours along with velocity vectors for different A-λ combinations for a Al-Cu alloy solidifying on horizontal uneven surfaces. Details of the numerical study are given in [4] and are not repeated here.

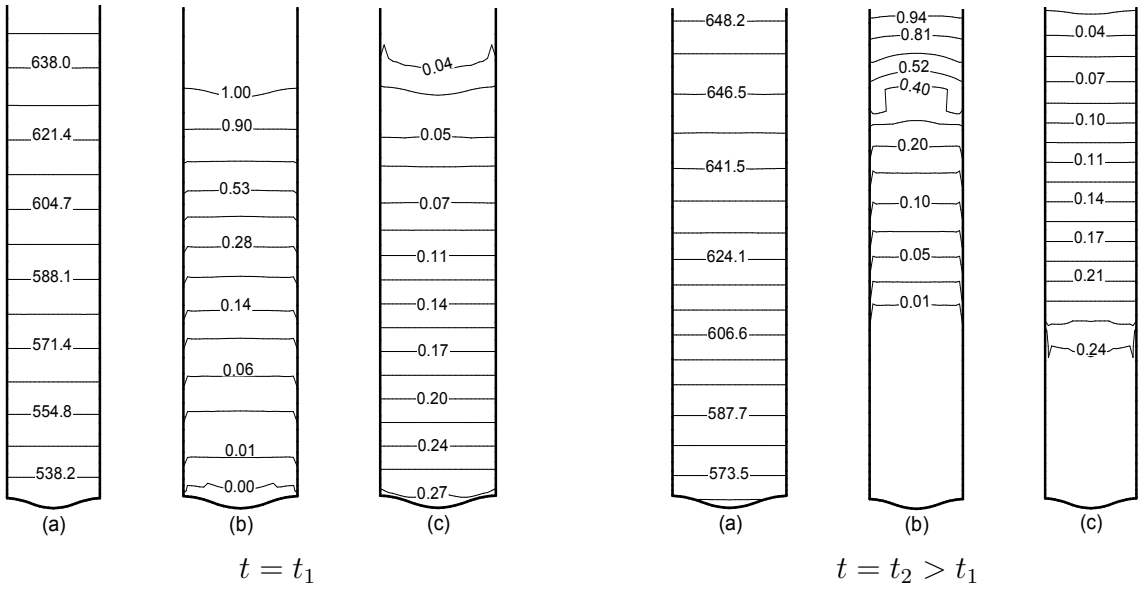

Figure 3: (a) Isotherms (b) liquid volume fraction (c) liquid concentration lines at $t_1 = 66\ s$ and $t_2 = 121\ s$ for vertical solidification with shrinkage ($\lambda = 10$ mm, $A = 0.5$ mm) in [4].

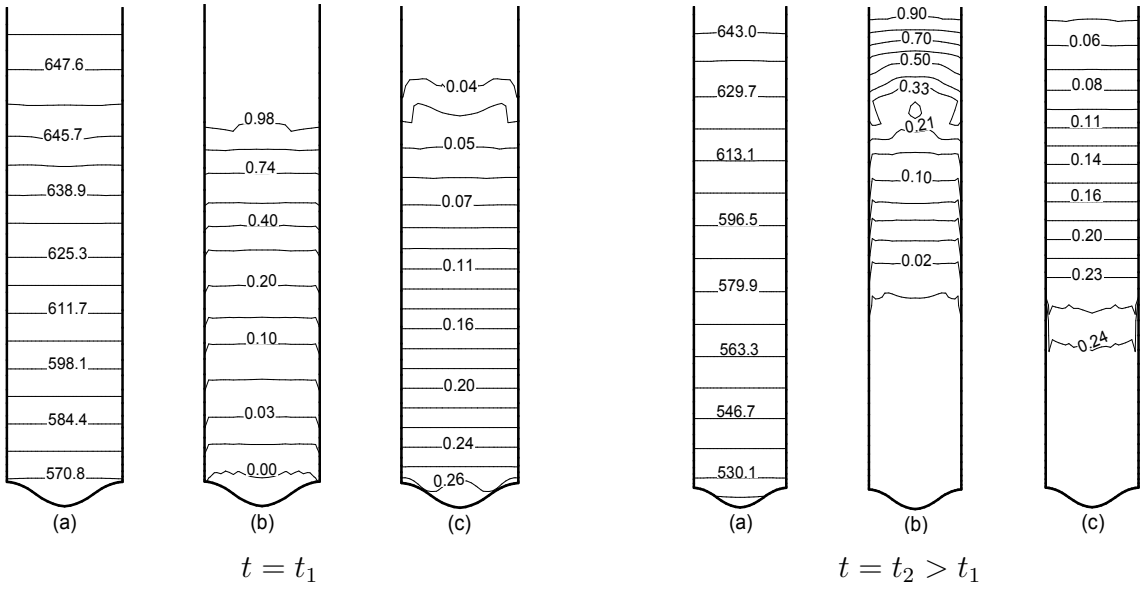

Figure 4: (a) Isotherms (b) liquid volume fraction (c) liquid concentration lines at $t_1 = 66\ s$ and $t_2 = 121\ s$ for vertical solidification with shrinkage ($\lambda = 10$ mm, $A = 1$ mm) in [4].

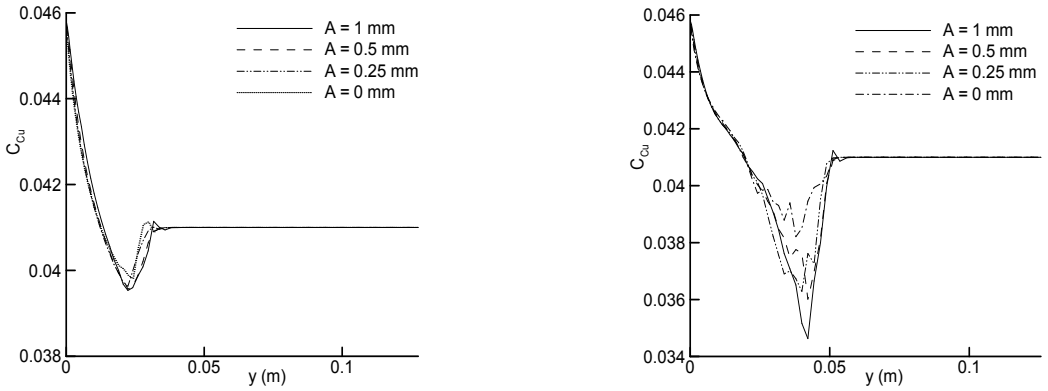

$t = t_1$ $\qquad$ $t = t_2 > t_1$

Figure 5: Midplane (x = 0.005 m) solute concentration profiles at $t_1 = 66$ s and $t_2 = 121$ s for different amplitudes at a fixed wavelength for vertical solidification with shrinkage ($\lambda = 10$ mm) in [4].

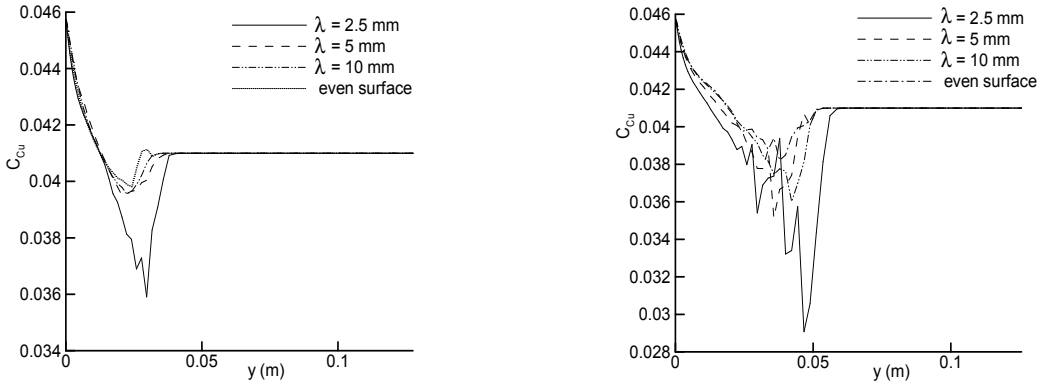

$t = t_1$ $\qquad$ $t = t_2 > t_1$

Figure 6: Midplane (x = 0.005 m) solute concentration profiles at $t_1 = 66$ s and $t_2 = 121$ s for different wavelengths at a fixed amplitude for vertical solidification with shrinkage (A = 0.5 mm) in [4].

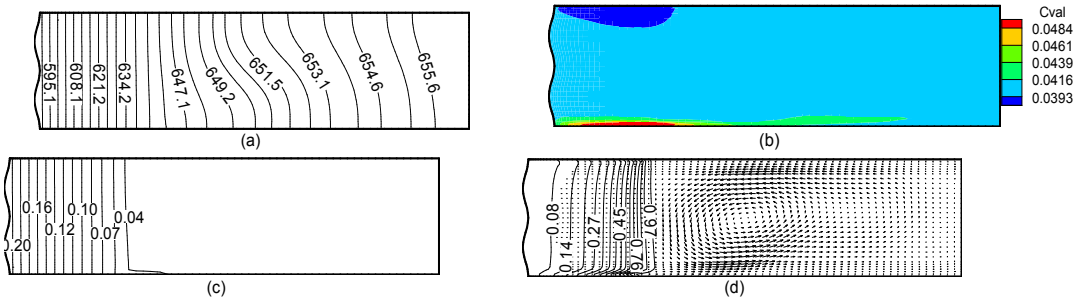

Figure 7: (a) Isotherms (b) solute concentration distribution (c) liquid solute concentration (d) liquid volume fraction and velocity distribution at time t = 66 s in horizontal solidification with $\lambda = 10$ mm and $A = 0.5$ mm, [4].

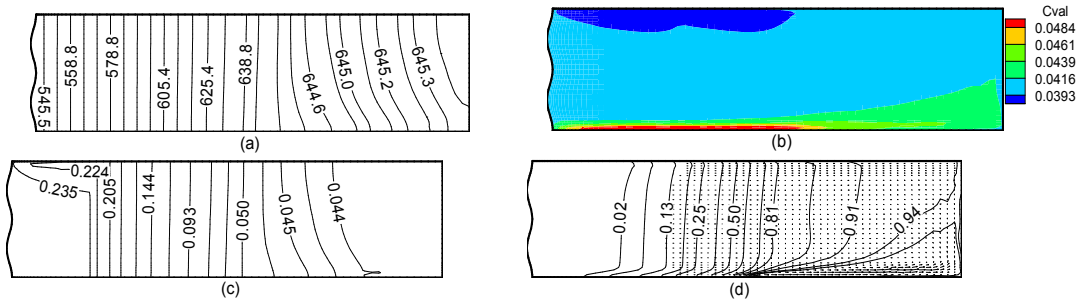

Figure 8: (a) Isotherms (b) solute concentration distribution (c) liquid solute concentration (d) liquid volume fraction and velocity distribution at time t = 121 s in horizontal solidification with $\lambda = 10$ mm and $A = 0.5$ mm, [4].

3.4 Deformation of solidifying alloys

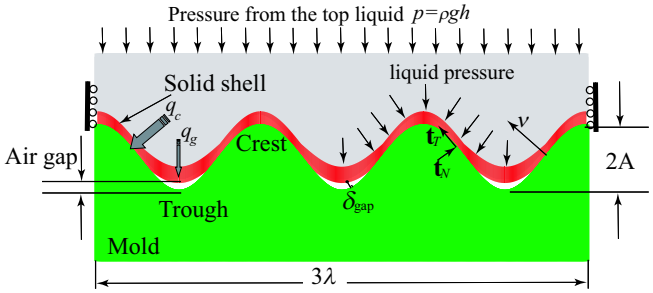

Figure 9: Alloy solidification from a mold with sinusoidal topography. The computational domain for the solid, mushy and liquid regions is only a small portion of the total domain considered due to emphasis on the early stages of solidification.

Here, the deformation of an Al-Cu alloy solidifying on molds of uneven topography was analyzed. A hypoelastic, rate-dependent model was used to describe deformation in the solidifying alloy. The mushy-zone was treated as a visco-plastic porous medium saturated with liquid [5]. The primary unknown in the displacement problem is the deformation vector, $\boldsymbol{u}$. Using a small-deformation assumption, the strain measure, $\boldsymbol{\varepsilon}$ is expressed as a sum of the elastic, plastic and thermal contributions as follows:

$$\boldsymbol{\varepsilon} \equiv \frac{1}{2}(\nabla \boldsymbol{u} + (\nabla \boldsymbol{u})^t) = \boldsymbol{\varepsilon}^e + \boldsymbol{\varepsilon}^p + \boldsymbol{\varepsilon}^T, \tag{11}$$

where $\boldsymbol{\varepsilon}^e$, $\boldsymbol{\varepsilon}^p$ and $\boldsymbol{\varepsilon}^T$ denote the elastic, plastic and thermal contributions, respectively, and are calculated through the volume-averaged model in the solid, liquid and mushy regions [6]. A hypoelastic law is used to express the stress-rate, in the whole domain, as:

$$\dot{\boldsymbol{\sigma}} = \mathcal{L}^e(\dot{\boldsymbol{\varepsilon}}^e), \tag{12}$$

where $\mathcal{L}^e \equiv 2\mu\mathcal{I} + (\kappa - \frac{2}{3}\mu)\mathbf{I} \otimes \mathbf{I}$, with μ and κ denoting Lame's constants. The thermal strain rate is calculated from the rates of change in temperature, T, and solid volume fraction, ϵ_s, as follows:

$$\dot{\boldsymbol{\varepsilon}}^T = \frac{w}{3}\left(\beta_{s,T}\dot{T} + \beta_{sh}\dot{\epsilon_s}\right)\mathbf{I}, \tag{13}$$

where $\beta_{s,T}$ is the coefficient of volumetric thermal expansion, β_{sh} is the coefficient of volumetric shrinkage calculated from phase densities and w is a function of the solid fraction. There is a

Table 1: Constitutive law of Aluminum copper alloy [5]

$$\mathcal{F} = \dot{\tilde{\varepsilon}}^p = \dot{\boldsymbol{\varepsilon}}_0 \left[\frac{\tilde{\sigma}}{\sigma_0} \exp(-\delta \epsilon_s) \cdot \exp\left(-\frac{mQ}{RT} \right) \right]^{1/m}$$

$\dot{\epsilon}_0$	σ	Q	m	δ
$9 \times 10^{-5} s^{-1}$	5.5 kPa	154 J/mol	0.4	6.3

critical solid fraction, ϵ_s^{crit}, below which thermal strain is zero [5]. Therefore, w is expressed as

$$w = \begin{cases} 0 & \text{for } \epsilon_s < \epsilon_s^{crit}, \\ 1 & \text{for } \epsilon_s \geq \epsilon_s^{crit}, \end{cases} \tag{14}$$

Non-zero thermal strain is produced in the solid-shell only when ϵ_s exceeds ϵ_s^{crit}, [5]. Below ϵ_s^{crit}, the developing mushy-zone has negligible strength and Eq. (14) reduces to

$$\dot{\boldsymbol{\varepsilon}}^T = 0. \tag{15}$$

As described in [6], this necessitates a constraint on the stress given by

$$\boldsymbol{\sigma}' = 0 \quad \text{if } \epsilon_s < \epsilon_s^{crit}, \tag{16}$$

where $\boldsymbol{\sigma}'$ is used here to denote the deviatoric part of the Cauchy stress

$$\boldsymbol{\sigma}' \equiv \boldsymbol{\sigma} - \frac{1}{3} tr(\boldsymbol{\sigma}) \mathbf{I}. \tag{17}$$

In the solid region, with $\dot{\epsilon}_s = 0$ and $w = 1$, Eq. (13) becomes

$$\dot{\boldsymbol{\varepsilon}}^T = \frac{1}{3} \beta_{s,T} \dot{T} \mathbf{I}. \tag{18}$$

The evolution of the plastic strain obeys the normality rule

$$\dot{\boldsymbol{\varepsilon}}^p = \frac{3}{2} \frac{\dot{\tilde{\varepsilon}}^p}{\tilde{\sigma}} \boldsymbol{\sigma}', \tag{19}$$

where $\dot{\tilde{\varepsilon}}^p$ is the equivalent plastic strain-rate and $\tilde{\sigma}$ the equivalent stress. The equivalent plastic strain evolution $\dot{\tilde{\varepsilon}}^p$ is specified through experiments as

$$\dot{\tilde{\varepsilon}}^p = \mathcal{F}(\tilde{\sigma}, s, T) = w \mathcal{F}_0(\tilde{\sigma}, s, T), \tag{20}$$

where $\mathcal{F}$ and $\mathcal{F}_0$ are scalar functions and w is defined as in Eq. (14) to account for the critical solid volume fraction. The evolution of the state variable, s (resistance to plastic deformation), is given by

$$\dot{s} = g(\tilde{\sigma}, s, T) = w g_0(\tilde{\sigma}, s, T), \tag{21}$$

and is also obtained from experiments. Eqs. (20) and (21) give a general framework of the constitutive law. The constitutive relationship, obtained from [5] and described in Table 1, is used in our numerical model. Values of important constants in the constitutive law are also

given in Table 1. In our current analysis, we assume the deformation process of the solidifying alloy to be quasistatic and the body to be under equilibrium at all times. The equilibrium condition of the solidifying body can then be written as

$$\nabla \cdot \boldsymbol{\sigma} + \rho g \boldsymbol{e_g} = 0 \tag{22}$$

where $\boldsymbol{e_g}$ denotes the gravity field. Eq. (22) is obtained after simplifying the volume-averaged momentum conservation equation and neglecting the effect of the liquid-phase pressure on the solid-phase momentum equation [5]-[7]. In the liquid and mushy-zones with $\epsilon_s < \epsilon_s^{crit}$, Eq. (22) leads to $\boldsymbol{\sigma} = -\rho g h \mathbf{I}$, since $\boldsymbol{\sigma'} = 0$. With this approach, the initial stress of a particle when it solidifies is assumed to be the hydrostatic pressure at that location [8]. This initial stress condition is important for tracking the history of deformation of solid particles once they solidify.

Modeling of contact tractions (normal $\boldsymbol{t_N}$ and tangential $\boldsymbol{t_T}$) and air-gaps between the casting and mold surfaces follows the scheme described in [9]. The mold separates the space into inadmissible (the mold region itself) and admissible (other regions) regions and is parameterized such that the normal vector $\boldsymbol{\nu}$ points into the admissible region. The gap size (Δ_{gap}) of any point in space is defined as the shortest distance from that point to the mold. Numerically, the contact force and gap size are solved using augmentations, details of which are given in [6] and not repeated here.

Imperfect contact between the solid-shell/mold interface significantly affects thermal conditions at that interface. This in turn affects fluid flow, segregation and solid-shell growth morphology. When air-gaps form between the solid-shell and mold surface, there is a decrease in heat flux. In our numerical model, we use two different heat flux formulations, described in [10, 11], to simulate the change in thermal boundary conditions caused by air-gap formation. These have been previously used in [6] and are expressed as follows:

$$q = \begin{cases} q_g = \frac{h_0}{1+\Delta_{\text{gap}} h_0/k_0}(T_{cast} - T_{mold}), \\ \text{if } \Delta_{\text{gap}} > 0 \\ q_c = \frac{1}{(R_0 + R' p_{contact})}(T_{cast} - T_{mold}), \\ \text{if } \Delta_{\text{gap}} = 0 \end{cases} \tag{23}$$

where Δ_{gap} is the air-gap size, $p_{contact}$ is the contact pressure between the mold and the solid-shell, T_{cast} and T_{mold}, are temperatures of the solid-shell and mold surfaces at the metal-mold interface, respectively. The parameters R_0, R', h_0 and k_0 are empirical coefficients [10, 11]. Actual values of these parameters are given in [6] and [12]. The heat fluxes q_g and q_c are schematically shown in Fig. 9.

3.5 Numerical Examples

In our initial numerical studies, the gap nucleation time during the solidification of pure aluminum on molds of varying sinusoidal topography was determined under different process conditions like melt pressure and mold materials. Further details of these examples are given in [6]. As shown in Figs. 10 (a) and (b), results obtained from our numerical model were compared with a semi-analytical solution for air-gap nucleation that was derived in [10],[13] and [14] by using a thermo-hypoelastic perturbation theory neglecting plastic deformation. Events after the gap nucleation are extremely important for understanding the surface-defect formation process. After completing the validation studies, solidification of an Al-Cu alloy was

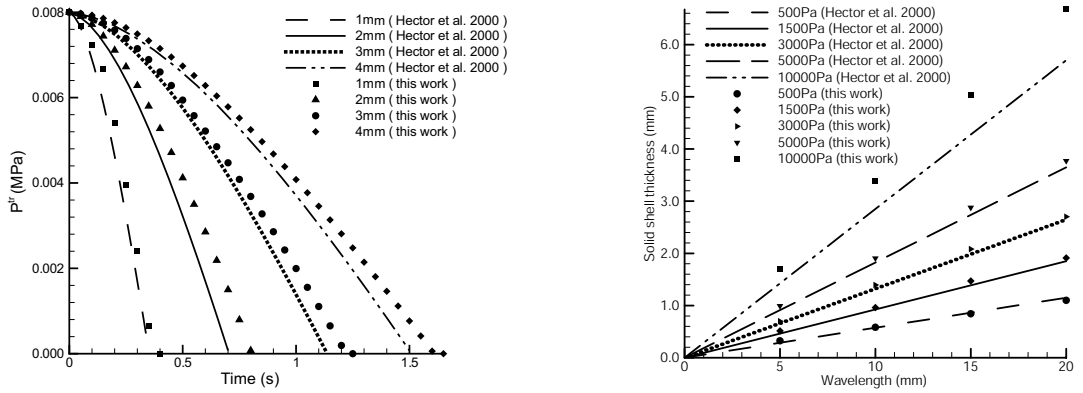

(a) (b)

Figure 10: (a) Evolution of P^{tr} with time at selected λ for pure aluminum (P_l=8000 Pa, R_0 = 10^{-3}m^2·sec·K/J) (b) Mean shell thickness at gap nucleation time as a function of mold wavelength for pure aluminum ($R_0 = 10^{-3}$m^2·sec·K/J), [6].

simulated in sinusoidal cavities, initially neglecting solute transport, [6]. Figs. 12 and 13 show results for two different mold topographies at times t = 5 ms and t = 100 ms. Micro sized air-gaps form at the metal-mold interface as solidification progresses leading to a non-uniform heat transfer rate into the casting. It is observed that the growth front unevenness decreases faster when the mold surface wavelength (λ) is 1 mm than when it is 5 mm.

Solidification of an Al-Cu alloy was then simulated in sinusoidal cavities with an amplitude, A and wavelength, λ after taking into account solute transport, [12]. The numerical model for alloy solidification was same as that described in Section . The domain and boundary conditions for the deformation and solidification problem are described in Fig. 9 and Fig. 2, respectively. We observe the effect of transport phenomena occurring near the metal-mold interface, on stress development, air-gap formation and growth morphology unevenness in the solid-shell. More details about the initial and boundary conditions used for different examples are given in [12]. Figs. 14-16 summarize results obtained for few $A-\lambda$ combinations for different process conditions with the emphasis on early stages of solidification. The left-half corresponds to the time t = 5 ms, while the right-half to t = 100 ms. In all examples considered here, inverse segregation, primarily induced by shrinkage driven flow, is observed at the bottom of the cavities (Figs. 14b-16b) leading to a non-uniform solute concentration. Air-gap nucleation occurs at the troughs and this leads to a local reduction in heat transfer out of the solidifying shell at these locations. Consequently, remelting occurs at the troughs and solid forms earlier at the crests than at the troughs as observed in Figs. 14d-16d at $t = 100$ ms. The process parameters that are varied in these examples are wavelength of sinusoidal surfaces (λ), melt superheat (ΔT_{sup}), mold material and initial solute (Cu) concentration (C_0) of the alloy. Figs. 17-19 show the transient development of maximum air-gap sizes and equivalent stresses for different wavelengths, melt superheat, Cu concentrations and mold materials, respectively. Maximum air-gap sizes were found to decrease with increasing ΔT_{sup}, decreasing λ and decreasing C_0, while maximum equivalent stresses decreased with decreasing λ but were relatively unaffected by ΔT_{sup} and C_0. The maximum equivalent stress at the dendrite roots is shown in Fig. 22(a) for different C_0 at $t = 100$ ms, for a fixed λ, ΔT_{sup} and mold material. Clearly, the peak value is observed for a Cu concentration of 1.8 %, which makes this particular alloy most susceptible to hot-tearing. This observation was previously made in [7]-[17] and verified in [6], where inverse segregation and solute transport were neglected.

With maximum equivalent stress and growth front unevenness as the criteria an optimal

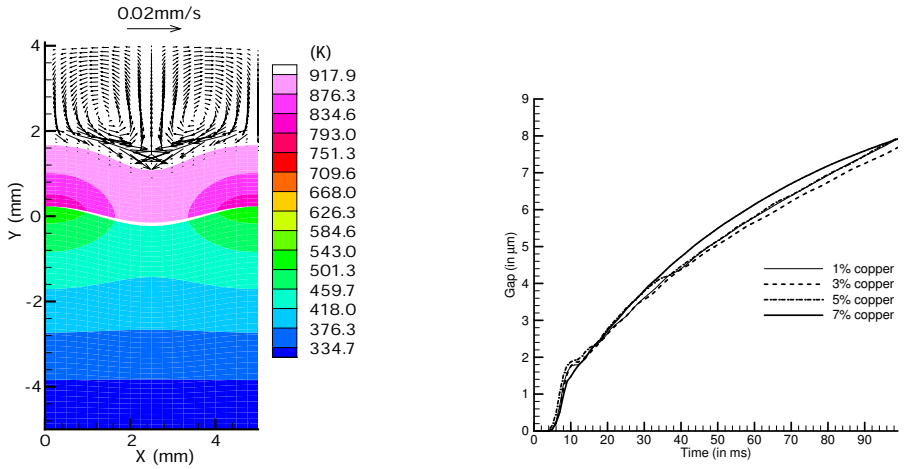

(a) (b)

Figure 11: (a) Temperature, flow and air-gap at time 100 ms for $\lambda = 5$ mm with superheat 30°C (the air-gap is magnified 20 times for easy visibility. (b) Evolution of the air-gap at the trough for different alloys ($\lambda = 5mm$ with 30°C superheat). The small bump around time 10 ms is due to remelting, [6].

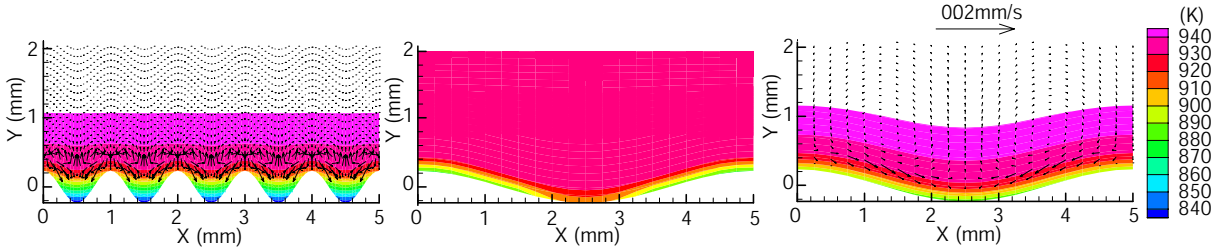

(a) (b) (c)

Figure 12: Temperature and flow velocity at time 5 ms: (a) $\lambda = 1mm$ with superheat 30°C, (b) $\lambda = 5\ mm$ without superheat, (c) $\lambda = 5\ mm$ with superheat 30°C, [6].

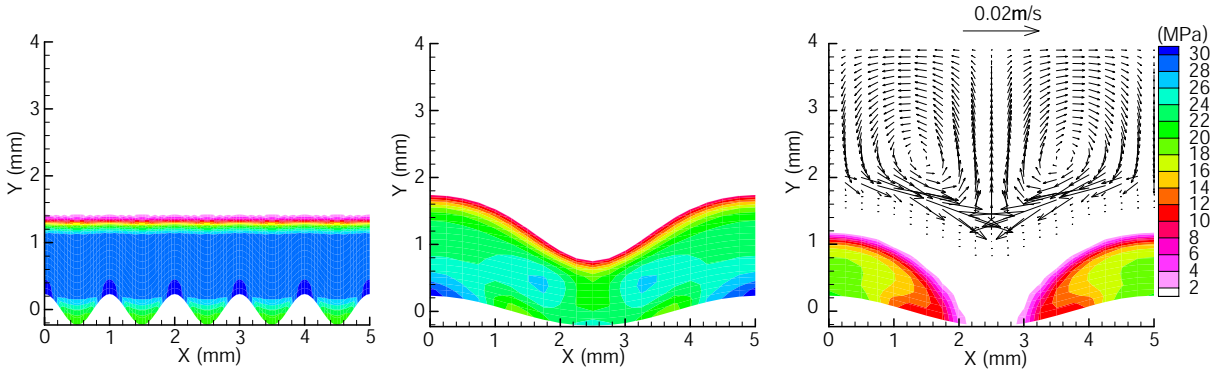

(a) (b) (c)

Figure 13: Equivalent stress and flow velocity at time 100 ms: (a) $\lambda = 1mm$ with superheat 30°C, (b) $\lambda = 5mm$ without superheat, (c) $\lambda = 5mm$ with superheat 30°C, [6].

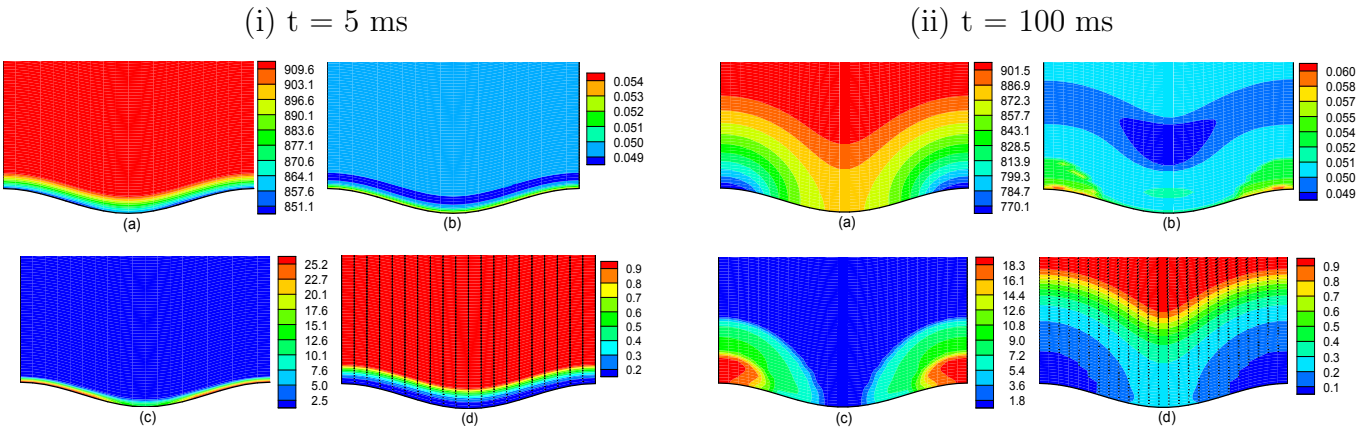

Figure 14: (a) Temperature in K (b) solute concentration (c) equivalent stress in MPa (d) liquid mass fraction and velocity vectors at (i) t = 5 ms ($|v|_{max} = 0.355$ m/s) and (ii) t = 100 ms ($|v_{max}| = 0.095$ m/s) for $\lambda = 5$ mm, $C_0 = 5\%$Cu and no superheat ($A = 0.232$ mm, mold material- copper).

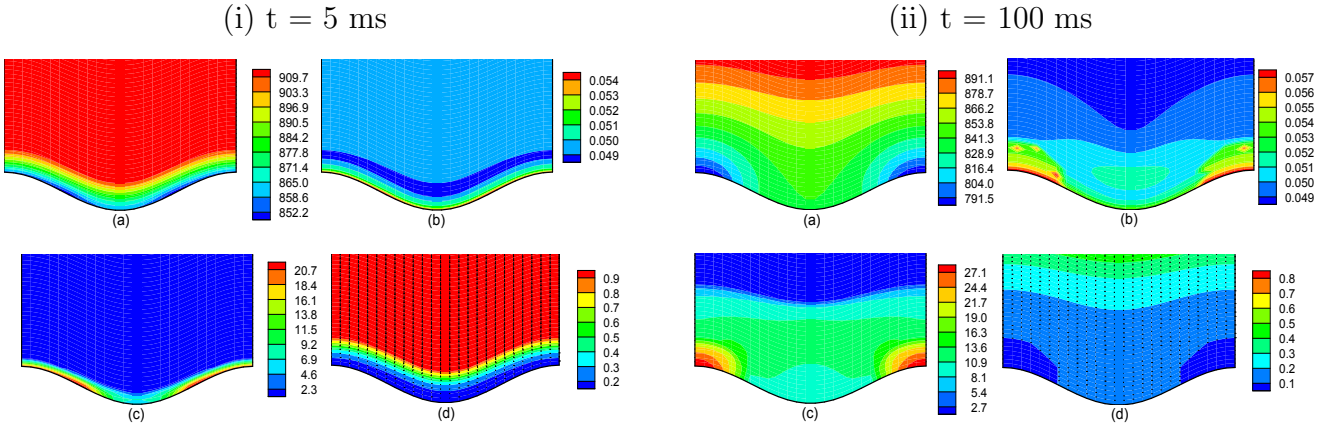

Figure 15: (a) Temperature in K (b) solute concentration (c) equivalent stress in MPa (d) liquid mass fraction and velocity vectors at (i) t = 5 ms ($|v|_{max} = 0.342$ m/s) and (ii) t = 100 ms ($|v|_{max} = 0.090$ m/s) for $\lambda = 3$ mm, $C_0 = 5\%$Cu and no superheat ($A = 0.232$ mm, mold material- copper).

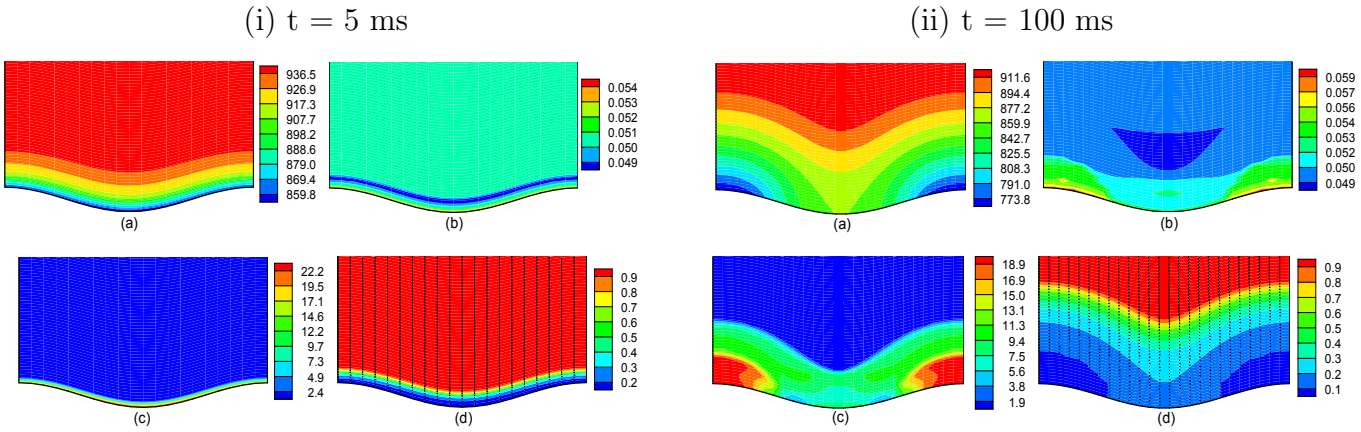

Figure 16: (a) Temperature in K (b) solute concentration (c) equivalent stress in MPa (d) liquid mass fraction and velocity vectors at (i) t = 5 ms ($|v|_{max}$ = 0.382 m/s) and (ii) t = 100 ms ($|v|_{max}$ = 0.096 m/s) for λ = 5 mm, C_0 = 5% Cu and 30^oC superheat (A = 0.232 mm, mold material - copper).

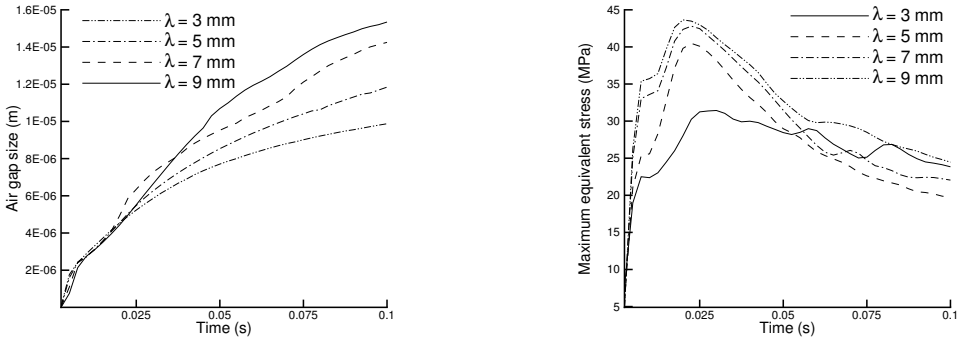

(a) (b)

Figure 17: (a) Variation of the maximum air-gap size as a function of time for different wavelengths (b) Variation of the maximum equivalent stress as a function of time for different wavelengths (Cu concentration = 5 %, melt superheat = 0^oC, mold material - Cu).

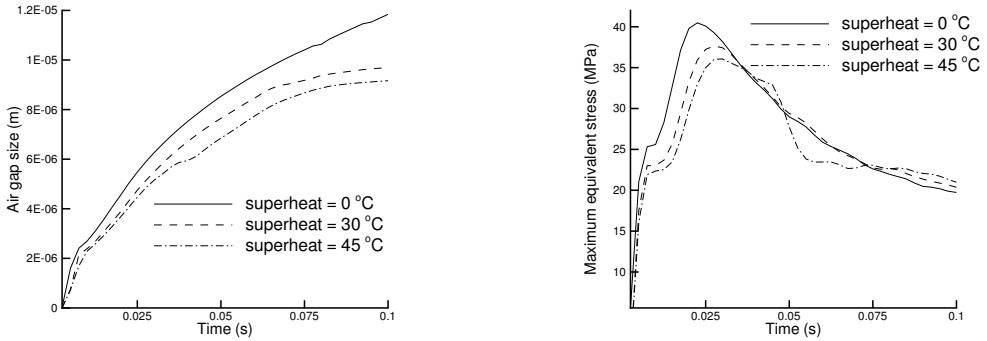

(a) (b)

Figure 18: (a) Variation of the maximum air-gap size as a function of time for different melt superheats (b) Variation of the maximum equivalent stress as a function of time for different melt superheat values (λ = 5 mm, Cu concentration = 5 %, mold material - Cu).

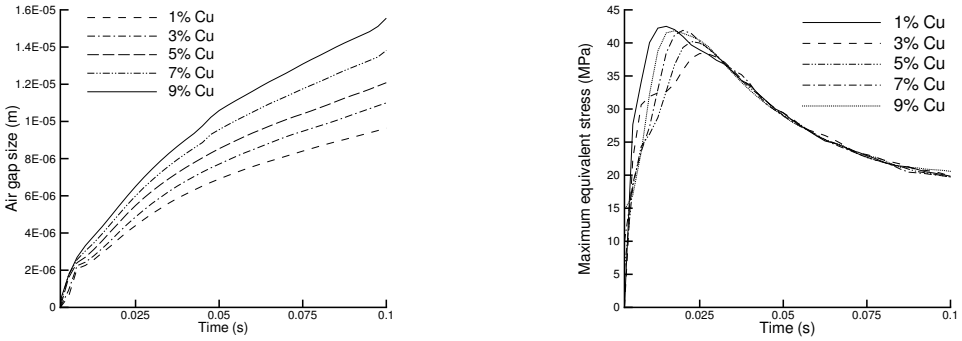

(a) (b)

Figure 19: (a) Variation of the maximum air-gap size at trough as a function of time for different solute (Cu) concentrations (b) Variation of the maximum equivalent stress as a function of time for different solute (Cu) concentrations ($\lambda = 5$ mm, melt superheat = 0^oC, mold material - Cu).

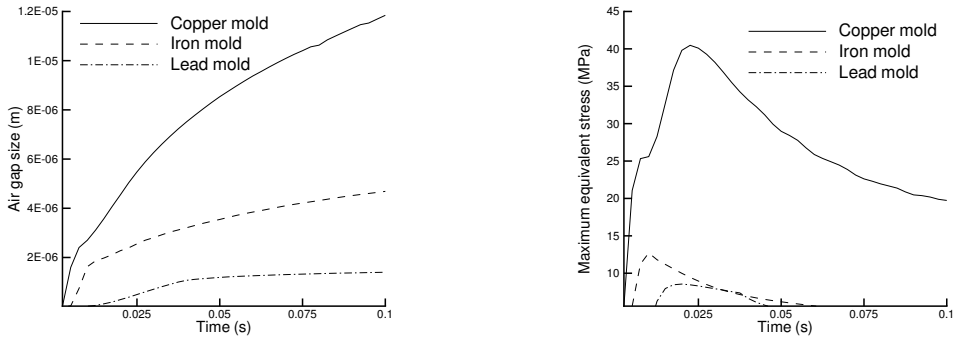

(a) (b)

Figure 20: (a) Variation of the maximum air-gap size as a function of time for different mold materials (b) Variation of the maximum equivalent stress as a function of time for different mold materials ($\lambda = 5$ mm, Cu concentration = 5 %, melt superheat = 0^oC).

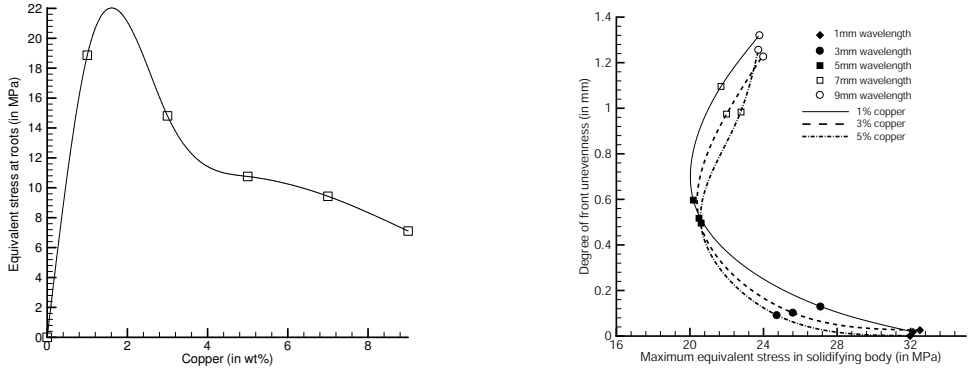

(a) (b)

Figure 21: (a) Maximum equivalent stress at roots of the dendrites for the Al-Cu system ($\lambda = 5$ mm with 30°C superheat, at time 100 ms). (b) Maximum equivalent stress in the solidifying body and front unevenness at an early solidification time (100 ms) (Solute transport neglected here).

wavelength range of slightly less than 5 mm was obtained that minimized both these quantities as shown in Figs. 21(b) and 22(b). The effect of inverse segregation was to increase the growth front unevenness of the solid shell and maximum air-gap sizes.

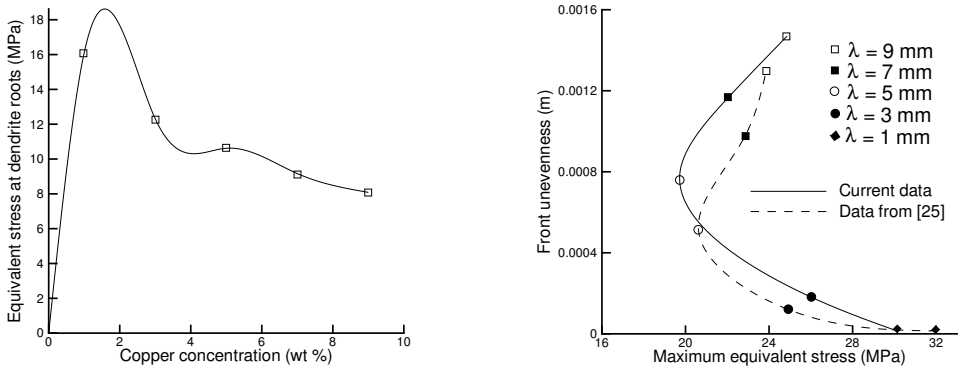

(a) (b)

Figure 22: Maximum equivalent stress in the solidifying alloy and front unevenness at $t = 100$ ms (melt superheat = 0^oC, Cu concentration = 5 %). From [6], the position difference of $\epsilon_l = 0.7$ corresponding to the crest and the trough is used here as a measure of front unevenness (in the presence of inverse segregation).

3.6 Effects of surface tension on early stage solidification

Modeling and simulation on the scale of surface roughness is important to understand the underlying physics of the complex phenomena at very early stages of chill casting including rapid cooling, solidification, and thermal distortion. Surface tension effects become important on these length scales. When molten aluminum contacts a chilled mold surface, the mold surface chemistry determines the contact condition between mold and molten metal. This contact condition plays an important role in the consequent solidification stages.

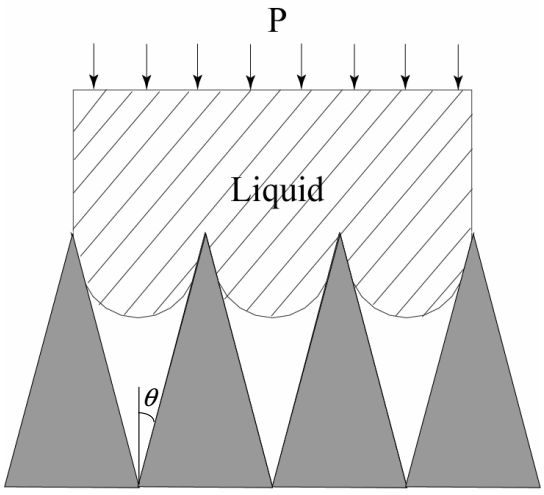

Figure 23: Contact between molten aluminum and mold surface.

When molten metal starts contact with mold surface under a certain liquid pressure P, typically an initial gap is formed as shown in Fig. 23. The software *Surface Evolver* was used

to calculate the state with minimum energy. This state with minimum energy was then deemed as the initial condition for the solidification process. The energy considered includes surface energy(free liquid surface and contact surface), prescribed pressure energy and gravitational potential energy. The surface energy is given by

$$E_{surface} = \int_{\partial\Omega} \sigma dS, \tag{24}$$

where σ is the surface energy per unit area. σ may take different values for different part of the liquid surface. For free liquid surface, σ takes the value of surface tension T. While at the part contact with mold surface, σ takes the value of $T\cos\theta_c$, where θ_c is the contact angle between liquid and mold surface. In the numerical implementation of surface evolver, this energy is calculated on every facet of the liquid body for the 3D model. In a two dimension model, the tension resides on edges instead of facets. The energy contribution from a liquid body with a prescribed pressure P is given by

$$E_{pressure} = \int_{\Omega} PdV = P\int_{\Omega} 1dV \tag{25}$$

For a free liquid surface, the mean curvature is determined by the value of pressure. In *surface Evolver*, there is no volume element. Integration over the body needs to be convert to surface integral according to Divergence Theorem. In our calculation, we use

$$E_{pressure} = P\int_{\Omega} 1dV = P\int_{\partial\Omega} z\vec{k}\cdot\boldsymbol{n}dS \tag{26}$$

With ρ as the density of the liquid, the gravitational energy contributed to the total energy is given by,

$$E_{gravity} = \int_{\Omega} G\rho z dV \tag{27}$$

Using divergence theorem, the volume integral is converted to a surface integral.

$$E_{gravity} = \int_{\partial\Omega} G\rho\frac{z^2}{2}\vec{k}\cdot\boldsymbol{n}dS \tag{28}$$

In the numerical implementation, this integral is done over each facet that bounds the liquid body.

The effects of surface tension, liquid pressure, gravity and mold topography are studied on the initial contact between molten metal and molds with a grooved surface.

Effects of surface tension: Fig. 24 shows the effect of varying mold wall surface tension, σ_{wall}, on the initial contact between the liquid and the mold. Near the melting temperature, the surface tension of molten aluminum is about $\sigma_{liquid} = 93\times10^{-3}J/m^2$. In practice, a coating is often applied at the mold surface to change the contact surface energy, so that better contact condition is achieved. In these cases, the amplitude $H = 10\mu m$, angle $\theta = 15^o$(Meaning of H and θ is shown in Figure 23) and the liquid pressure is chosen to be $P = 1.0\times10^4 Pa$.

Effects of liquid pressure: Fig. 25 shows the effect of verying liquid pressure for the same geometry (amplitude $H = 10\mu m$, angle $\theta = 15^o$) and with $\sigma_{liquid} = 1.0\sigma_{wall}$. The contact surface area between the liquid and the mold increases with increase in liquid pressure. Therefore, a large liquid pressure is preferable to improve heat transfer at the very early stages of solidification. Strictly, the pressure is not constant near the mold surface.

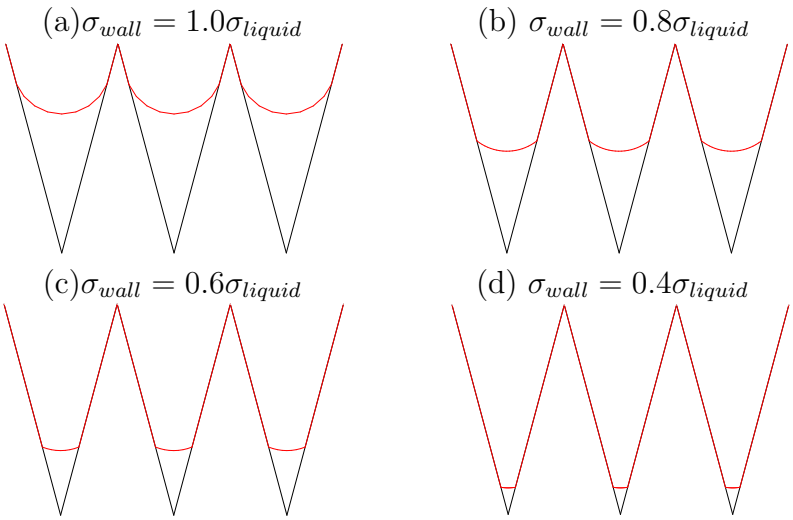

Figure 24: Effect of surface tension on the initial molten metal-mold wall contact.

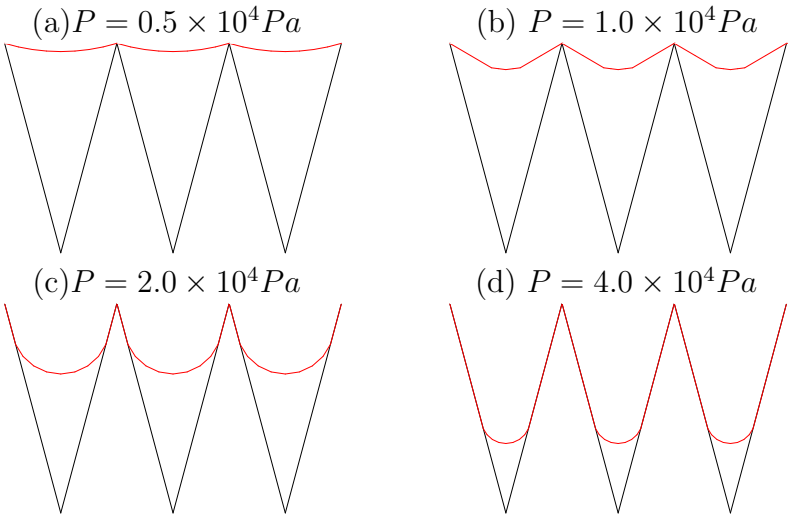

Figure 25: Effect of liquid pressure on the initial molten metal-mold wall contact.

Effects of gravity: We studied a case of a droplet of molten aluminum in contact with a V shaped mold, as shown in Fig. 26, to study the effects of gravity. In this case, $\sigma_{wall} = 1.0\sigma_{liquid}$, volume of droplet $V = 100mm^3$, V-shape height $H = 1.1mm$ and V-shape angle $\theta = 45^o$. Presence of gravity changes the initial shape of the droplet (a sphere) and increases its contact surface area with the mold surface. This improves heat transfer at early stages of solidification.

Effects of mold topography: Fig. 27 shows the effect of mold surface topography on the initial contact condition between molten aluminum and mold surface. In all these cases, the amplitude was $H = 10\mu m$, mold surface tension $\sigma_{wall} = 1.0\sigma_{liquid}$ and liquid pressure $P = 10^4 Pa$.

3.7 Solidification on a substrate

Taking the state with minimum energy as the initial condition for solidification, we computed solidification on a substrate for different surface tensions due to coating as shown in Fig. 28. As observed previously, the solid growth occurs from the crest. This method is valid for sand

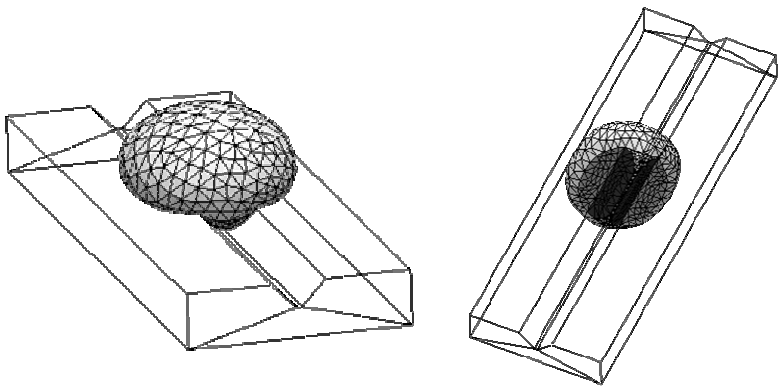

Figure 26: Effect of gravity on the initial molten metal-mold wall contact.

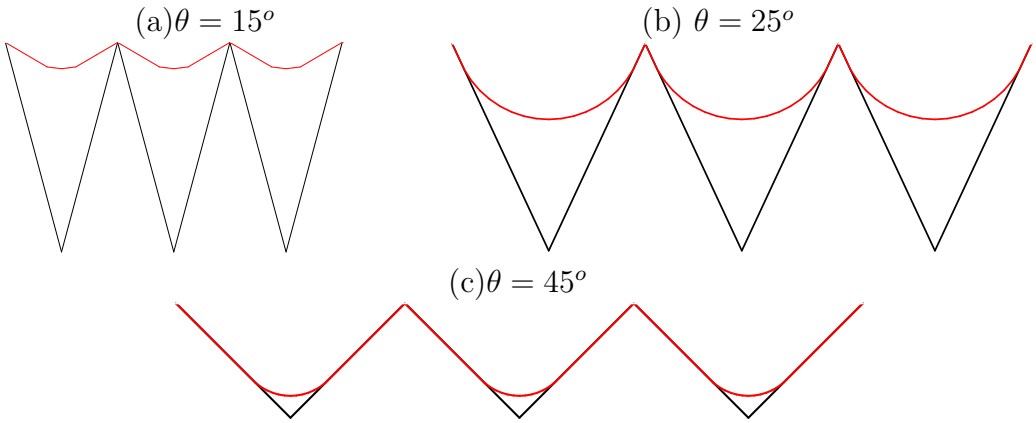

Figure 27: Effect of mold topography on the initial contact between the molten metal-mold wall contact.

casting, where gas escapes. However for metal mold casting, the gas is often trapped. Temperature change leads to gas pressure change. Numerically capture this phenomena requires the ability to handle multi-phase motion. We use the multi-phase level set method as the mathematical tool [15]-[16]. In this method, the phase boundary for each phase is not explicitly tracked with a mesh as in Surface Evolver. Phase boundary position is implied in the signed distance function.

$$\phi_\alpha(x,t) = \begin{cases} +d(x,t) & x \notin \Omega_\alpha \\ 0 & x \in \Gamma_\alpha \\ -d(x,t) & x \in \Omega_\alpha \end{cases}$$

Assuming liquid is at its equilibrium shape with minimum energy at each time step, the system energy can be written in the following form:

$$E = \int_\Omega \underbrace{\sum_\alpha \delta(\phi^\alpha)\gamma^\alpha}_{\text{surface energy}} + \underbrace{H(\phi^l)\left(\Delta P + \rho^l g^l h\right)}_{\text{pressure\&gravity potential energy}} \, dx$$

Using the gradient projection method, the energy minimization problem can be restated as:

$$\frac{\partial \phi^l}{\partial t} = \left[\gamma_l \kappa_l - \left(\Delta P + \rho^l h g^l\right) - \lambda\left(\sum_\beta H(\phi^\beta) - 1\right)\right], \frac{\partial \phi^g}{\partial t} = \left[\gamma_g \kappa_g - \lambda\left(\sum_\beta H(\phi^\beta) - 1\right)\right]$$

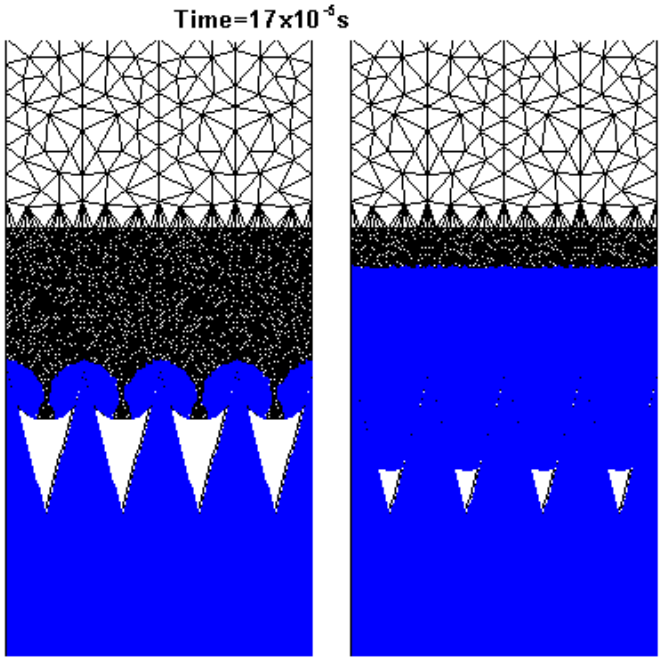

Figure 28: Effect of surface tension on early stage solidification.

with

$$\lambda = \frac{-\left(\sum_{\beta} H(\phi^{\beta}) - 1\right) \sum_{\alpha} \int_{\Omega} \delta(\phi^{l}) \left[-\gamma^{l}\kappa^{l} + \left(\Delta P + \rho^{l} h g^{l}\right)\right] + \delta(\phi^{g}) \left(-\gamma^{g}\kappa^{g}\right) dx}{\sum_{\alpha} \int_{\Omega} \delta(\phi^{\alpha}) \left(\sum_{\beta} H(\phi^{\beta}) - 1\right)^{2} dx}.$$

Fig. 29 shows the adaptive computational domain used for this problem. Simulation results show that initially the gas pressure increased due to increase in temperature, which pushed the liquid back. Gas escaped when the liquid was above the crest. The gas pressure then decreased due to decrease in temperature. Liquid contacted the mold again. Solidification started accompanied with liquid surface shape change due to surface tension until the bottom side of liquid became fully solidified.

3.8 Conclusions

The current project has successfully developed finite element based numerical techniques to model aluminum alloy solidification on uneven surfaces in the presence of non-uniform heat transfer and imperfect contact at the metal-mold interface. Through a full scale parametric analysis using this techniques, optimal surface topographies that helped in reducing some surface defects during early stage solidification of aluminum alloys were identified. The analysis, initially done on a macro scale, was extended to a micro scale to incorporate effects of surface tension. Level set methods, developed for modeling dendritic alloy solidification, were extended to model the effect of surface tension on early stage alloy solidification on a micro length scale.

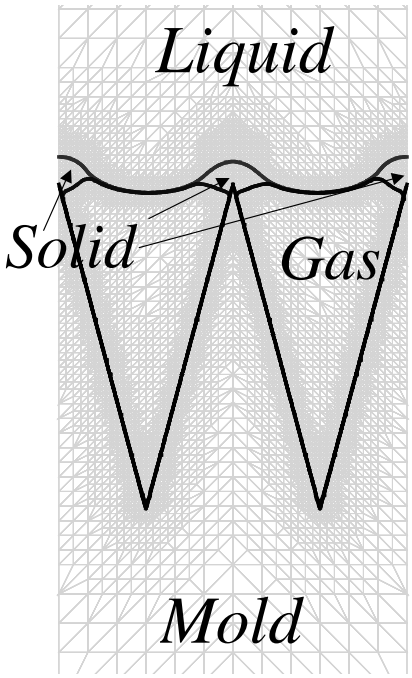

Figure 29: Substrate solidification in the presence of surface tension and gas pressure.

List of publications:

1. N. Zabaras and D. Samanta, 'Stabilized volume averaging finite element method for flow in porous media and binary alloy solidification processes', *Int. J. Num. Meth. Engr.*, Vol. 60(6), 1103-1138, 2004.

2. D. Samanta and N. Zabaras, 'Solidification and macrosegregation in aluminum alloys on uneven surfaces', proceedings of the 2004 TMS annual meeting and exhibition exhibition, Charlotte, North Carolina, March, 2004.

3. L. Tan and N. Zabaras, 'Modelling the effects of mold topography on aluminum cast surfaces', proceedings of the 2004 TMS annual meeting and exhibition, Charlotte, North Carolina, March, 2004.

4. D. Samanta and N. Zabaras, 'Modeling melt convection in solidification processes using stabilized finite element techniques', *Int. J. Num. Meth. Engr.* in press, 2005.

5. D. Samanta and N. Zabaras, 'Numerical study of macrosegregation in aluminum alloys solidifying on uneven surfaces', *Int. J. Heat Mass.Trans.*, Vol. 48, 4541-4556, 2005.

6. L. Tan and N. Zabaras, 'An energy conserving level set simulation of dendritic solidification with convection', *J. Comp. Phys.*, Vol. 211, 36-63, 2006.

7. L. Tan and N. Zabaras, 'A thermomechanical study of the effects of mold topography on the solidification of aluminum alloys', *Mat. Sci. Engr. A*, Vol. 211, 36-63, 2005.

8. D. Samanta and N. Zabaras, 'A coupled thermomechanical, thermal transport and segregation analysis of solidification of aluminum alloys on molds of uneven topographies', *Mat. Sci. Engr. A*,in press.

9. L. Tan, D. Samanta and N. Zabaras, 'A coupled thermomechanical, thermal transport and seg-

regation analysis of the solidification of aluminum alloys on molds of uneven surface topographies', presented in the Third M.I.T Conference on Computational Mechanics,Cambridge, Massachusets, June, 2005.

10. L. Tan and N. Zabaras, 'Level set method for simulating multi-phase multi-component dendritic solidification', presented in the Third M.I.T Conference on Computational Mechanics, Cambridge, Massachusets, June, 2005.

11. D. Samanta and N. Zabaras, 'Freckle suppression in directional solidification of binary and multicomponent alloys using magnetic fields', presented in the Third M.I.T Conference on Computational Mechanics, Cambridge, Massachusets, June, 2005.

12. L. Tan and N. Zabaras, 'An energy conserving level set simulation of dendritic solidification including the effects of melt convection', presented in the Eight U.S. National Conference on Computational Mechanics, University of Texas Austin, Texas, July 2005.

Budget Data:

			Approved Spending Plan			Actual Spent to Date		
Phase / Budget Period			DOE Amount	Cost Share	Total	DOE Amount	Cost Share	Total
	From	To						
Year 1	9/1/02	8/31/03	100,000	20,000	120,000	100,000	20,000	120,000
Year 2	9/1/03	8/31/04	100,000	15,000	115,000	100,000	15,000	115,000
Year 3	9/1/04	8/31/05	100,000	20,000	120,000	100,000	20,000	120,000
Totals								

References

[1] D.A. Weirauch Jr., A. Giron, Proc. Integration of Material, Process and Product Design, A.A. Balkema publ., Rotterdam, Netherlands, 183-191.

[2] D. Samanta, N. Zabaras, Modeling convection in solidification processes using stabilized finite element techniques, Int. J. Numer. Meth. Engr., in press, 2005.

[3] N. Zabaras, D. Samanta, A stabilized volume-averaged finite element method for flow in porous media and binary alloy solidification processes, Int. J. Numer. Meth. Engr.,60 (6) (2004), 1103-1138.

[4] D. Samanta and N. Zabaras, Numerical study of macrosegregation in aluminum alloys solidifying on uneven surfaces, *Int. J. Heat. Mass Trans.*, 48 (2005), 4145-4156.

[5] A. Strangeland, A. Mo, Ø. Nielsen, D. Elskin and M. Hamdi, Development of thermal strain in the coherent mushy zone during solidification of aluminum alloys, Metall. Mater. Trans. A 35 (2004) 2903-15.

[6] L. Tan, N. Zabaras, A thermomechanical study of the effects of mold topography on the solidification of Aluminum alloys, Mat. Sci. Engr. :A, 404 (2005), 197-207.

[7] I. Farup, A. Mo, Two-phase modeling of mushy zone parameters assosicated with hot tearing, Metall. Mater. Trans. A 31 (2000) 1461-1472.

[8] N. Zabaras, Y. Ruan, O. Richmond, Front tracking thermomechanical model for hypoelastic-viscoplastic behaviour in a solidifying body, Comp. Meth. App. Mech. and Eng. 81 (1990) 333-364.

[9] T. Laursen, *Computational Contact and Impact Mechanics*, Springer-Verlag Berlin Heidelberg, 2002.

[10] L.G. Hector Jr., J. Howarth, O. Richmond, W. Kim, Mold surface wavelength effects on gap nucleation in solidification, J. App. Mech. 67 (2000) 155-159.

[11] A. Bejan, *Heat Transfer*, John Wiley & Sons, Inc. 1993.

[12] D. Samanta and N. Zabaras, A coupled thermomechanical, thermal transport and segregation analysis of solidification of aluminum alloys on molds of uneven topographies, *Mat. Sci. Engr.:A*, in press.

[13] F. Yigit, L.G. Hector Jr., Critical Wavelengths for Gap Nucleation in Solidification Part I: Theoretical Methodology, J. App. Mech. 67 (2000), 66-76.

[14] F. Yigit, L.G. Hector Jr., Critical Wavelengths for Gap Nucleation in Solidification Part II: Results for Selected Mold-Shell Material Combinations , J. App. Mech. 67 (2000), 77-86.

[15] L. Tan and N. Zabaras, An energy conserving level set simulation of dendritic solidification with convection, *J. Comp. Phys.*, Vol. 211, 36-63, 2006.

[16] L. Tan and N. Zabaras, A level set simulation of dendritic solidification of multi-component alloys, *J. Comp. Phys.*, in preparation.

[17] M. Rappaz, J. Drezet, M. Gremaud, A new hot-tearing criterion, Metall. Mater. Trans. A 30 (1999) 449-455.